INDUSTRIAL ROBOTS

# Foldable and rollable interlaced structure for deployable robotic systems

**Sun-Pill Jung[1]†, Jaeyoung Song[1]†, Chan Kim[1], Haemin Lee[1,2], Inchul Jeong[1], Jongmin Kim[1], Kyu-Jin Cho[1]***



**Extendable structures often use rollable designs, with long, flexible materials that can be wound onto a hub for storage without the need for joints. However, achieving high stiffness and strength in the extended state while keeping the hub compact is challenging, given that stiff structures are difficult to bend and typically require larger hubs for storage. Here, we introduce a corrugated sheet–shaped foldable design that enables Z-folding by connecting multiple strips in parallel. The unfolded, corrugated form structure offers a high load-bearing capacity, and the folded, stacked form structure can be smoothly rolled onto a hub, enabling fold-and-roll storage. The key innovation is the formation of an interlaced origami structure by connecting strips through a ribbon-weaving technique. This interlacing design enables both localized flexibility and mutual constraints between strips: The localized flexibility accommodates perimeter differences between stacked strips during rolling, and the densely repeated mutual constraints make the corrugation resist excessive deformation under external forces. Using these structures, we made two deployable mobile robots: one with a 1.6-meter deployable arm for shelving tasks and another with a tetrahedral deployable frame that supported a meter-scale 3D-printing system. Our results showcase the potential of this interlaced, corrugated approach for deployable robotic systems requiring both compactness and strength.**

## INTRODUCTION

Extendable mechanisms allow expansion along a single axis. When the extended structures meet the required extended length and mechanical properties, these mechanisms help robotic systems overcome reachability limitations and enhance functionality (*1*–*13*). For practical applications, two key requirements must be satisfied: achieving compact storage through efficient geometric design and maintaining strong mechanical properties in the deployed state (*14*).

Rolling mechanisms (*15*–*21*), which store the structure by rolling it onto a hub, are often used to achieve compact storage. Typically, rollable structures adopt corrugated sheet designs that provide stiffness in a direction perpendicular to the corrugation. During storage, flattening the structures and removing the grooves make them suitable for rolling onto a hub ("Flattening and rolling conditions for storage without plastic deformation" section in the Supplementary Methods). For example, the storable tubular extendable member (STEM) (*15*), which has a slit circular tube cross section, is flattened into a single-layer sheet, and the triangular retractable and collapsible (TRAC) boom (*19*), composed of two tape springs bonded along one longitudinal edge, is flattened into a double-layered sheet. These rolling mechanisms leverage material compliance (*22*, *23*) rather than traditional mechanical joints, so they are advantageous in avoiding the rattling issues associated with joint clearance in linkage-based systems (*2*, *24*).

To achieve high mechanical performance in the extended state, the structure must form a robust corrugated shape with a high second moment of area. Because the width of the flattened structure must be smaller than the hub's height, maximizing the second moment of area within the given flattened width becomes a key design consideration. Therefore, many structural designs adopt a multilayer stacking strategy that enables larger and longer corrugated cross sections. Compared with the single-layer STEM, the double-layered TRAC boom, known as one of the rollable structures with high bending stiffness, can achieve an ~34-times greater second moment of inertia when both are flattened to the same width (*19*). However, in layer-bonded structures such as TRAC, increasing the number of layers introduces perimeter differences between the layers during rolling (*17*–*21*). These differences can result in inner-layer buckling (*16*, *25*) and ultimately lead to structural failure ("Challenges in rolling the stacked form structure" section in the Supplementary Methods). Consequently, it is hard to increase the number of layers in layer-bonded structures, so the hub dimension often limits the maximum achievable stiffness ("Relations between the achievable stiffness and the hub dimension" section in the Supplementary Methods).

To resolve the issue of perimeter differences in multilayered structures, slide-enabling joints instead of bonding have been proposed for connecting layers ("Mitigating perimeter difference through sliding motion" section in the Supplementary Methods). The sheath-based rollable lenticular-shaped and low-stiction (SHEARLESS) boom (*26*, *27*) is a tubular structure that is composed of two tape springs enclosed in a thin sheath. Because tape springs are not bonded, they can slide relative to each other in the sheath, enabling smooth rolling without internal stress from perimeter mismatches. The "slipping folds" approach (*28*, *29*) connects adjacent layers via sliding hinges with extended spacing between the knuckles, allowing the hinge leaves to fold and slide relative to one another. By matching the knuckle spacing to the length differences between layers during rolling, even multilayered structures can be rolled smoothly. Although these approaches substantially improve compact storage of multilayered structures, they have limitations: The SHEARLESS boom lacks

[1]Biorobotics Laboratory, Soft Robotics Research Center, Institute of Advanced Machines and Design, Department of Mechanical Engineering, Institute of Engineering, Seoul National University, Seoul 08826, Republic of Korea. [2]Mand.ro Co., Ltd., Bucheon 14557, Republic of Korea.
†These authors contributed equally to this work.
*Corresponding author. Email: kjcho@snu.ac.kr

scalability because of its fixed two-layer configuration, and the wide spacing of slipping folds weakens the robustness of the corrugation, making it difficult to achieve high load-bearing capacity. Therefore, to meet the dual demands of compact storage and structural performance for terrestrial robotic applications, our work aims to propose a structural design that achieves both a high second moment of area and a high load-bearing capacity even under compact hub dimensions.

Here, we developed the fold-and-roll corrugated structure (FoRoGated-Structure), an interlaced origami design in which multiple strips are connected in parallel through a ribbon-weaving technique (Movie 1). This interlacing design improves the connections between strips, providing localized flexibility in one direction for sliding while maintaining dense mutual constraints in the other for structural stability. The localized flexibility enables smooth and compact rolling of multiple stacked layers, and the dense constraints help preserve the corrugated cross-sectional shape under external loads. As a result, these dual characteristics of interlacing designs allow the structure to support heavier payloads while maintaining compact storage. To demonstrate the capabilities of the FoRoGated-Structure, we present two mobile robotic systems: a compact mobile robot in which the FoRoGated-Structure functions as a deployable robotic arm and a deployable mobile robot whose deployable frame was assembled from multiple FoRoGated-Structures. The first compact mobile robot, comparable in size to a robotic vacuum cleaner, features a 1.6-m extendable arm that allows it to perform shelving tasks in a human workspace. The second deployable mobile robot transforms its frame from a 0.7-m-high triangular column into a 3.4-m-high tetrahedral frame. Upon deployment, the frame successfully carried a 3D-printing system at the tip and completed printing tasks, constructing a 2.5-m-tall structure. This demonstration highlights the potential of the FoRoGated-Structure to enhance the reach and load capacity of robotic systems while achieving compact storage.

## RESULTS

### FoRoGated-Structure

Figure 1A illustrates the concept of the FoRoGated-Structure, where the folded structure rolled for compact storage and unfolded into a corrugated form during deployment. This design closely resembles foldable origami structures, which consist of facets and fold lines.

Origami, originating as the art of paper folding in Japan, has broadly influenced engineering applications (*30*–*35*). From an engineering perspective, the fold lines in origami structures not only are single rotational joints but also function as dense arrays of parallel rotational joints that share the same axis. In engineering origami structures, fold lines are typically implemented using compliant materials or flexible designs, with rigid facets joined to these fold lines (*36*–*38*). This configuration maintained a dense arrangement of rotational joints, enabling adjacent facets to tightly constrain each other's movements. Such dense mutual constraints enhanced the structure's load-bearing capacity and its ability to withstand substantial forces, such as the perpendicular folding principle (*13*). Movie S1 demonstrates an origami-inspired engineering structure made of polyethylene terephthalate (PET), with fold lines created by cutting. The video highlights how the density of mutual constraints among facets affected the structure's strength. Sparse mutual constraints resulted in local buckling occurring more easily, thereby severely weakening the structure.

Similarly, to withstand large external forces in its corrugated form, adjacent strips had to be interconnected through a dense array of parallel constraints. In other words, the structure had to maintain dense mutual constraints between facets, regardless of the amount of sliding required because of perimeter differences. To effectively decouple sliding motion from the density of mutual constraints, we developed an interlaced origami design that wove two strips together with a ribbon (Fig. 1B and movie S2). The ribbon's alternating path created a parallel-repeated interjoint between the strips. These interjoints, formed without bonding, effectively decoupled sliding


**Movie 1. Overview of an interlaced-origami rollable structure for compact fold-and-roll storage and high load capacity.**

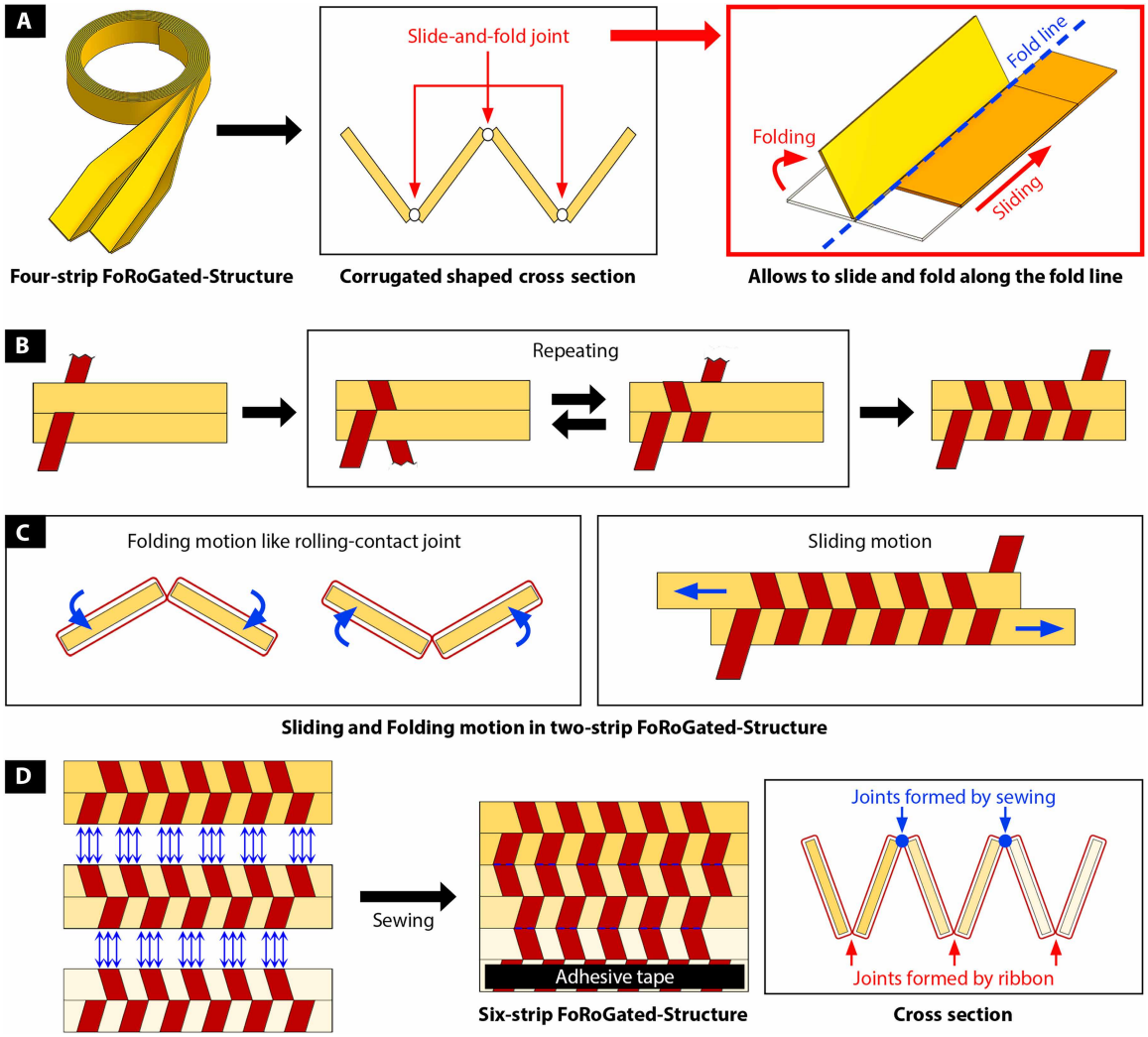


**Fig. 1. Concept of the FoRoGated-Structure and schematics of the fabrication method.** (**A**) Example of the FoRoGated-Structure and how slide-and-fold joints locate and work. (**B**) Ribbon-weaving method that fabricates the two-strip FoRoGated-Structure. (**C**) Sliding and folding motion in the two-strip FoRoGated-Structure. (**D**) Sewing method for the multistrip FoRoGated-Structure and its cross-sectional shape.

motion and folding motion: The strips folded like rolling-contact joints through the ribbon's bending (*39*) and slid smoothly through the gaps created by the ribbon's alternating path (Fig. 1C and movie S3). This design enabled the structure to accommodate substantial sliding while maintaining the density of interjoints. Thus, the interlacing approach kept the corrugated shape stable under external forces by suppressing local buckling while also offering localized flexibility for fold-and-roll storage.

In this design approach, ensuring consistent clearance between the ribbon and the strips was critical for smooth sliding. In our proposed weaving method, a unit pattern was defined, and the ribbon length in each unit pattern remained constant ("Detailed description of the FoRoGated-Structure" section in the Supplementary Methods). Consequently, the ribbon formed a loop of fixed length that the strips slid through, and this fixed loop length was preserved as long as the ribbon pattern remained undistorted. When two strips were inserted into the loop, the allocated clearance was equally distributed between them, making it unlikely for only one strip to become stuck. In contrast, if more than two strips were inserted into the loop, the allocated gap for each strip could vary depending on their relative positions. This uneven distribution of space could cause one of the strips to get stuck rather than slide freely. Therefore, we defined the two-strip FoRoGated-Structure as the basic unit and achieved multistrip configurations by sewing multiple two-strip units (Fig. 1D). This method made interlacing properties remain intact even when multiple two-strip units were connected in series (movie S4). In addition, because distortion of the woven pattern might have reduced the loop length, we affixed the ribbon to the outermost strip using tape. This method helped preserve the original woven pattern. For further details, see Materials and Methods for the fabrication method.

In summary, the multistrip FoRoGated-Structure achieved two key characteristics through the interlacing approach. During storage, it could be smoothly rolled onto a hub of consistent size, regardless of the number of stacked strips; when extended, it transformed

into a robust corrugated form through the dense mutual constraints between the strips.

### Extendable mechanism using the FoRoGated-Structure

Figure 2A illustrates the concept of an extendable mechanism for the FoRoGated-Structure, similar to conventional rollable mechanisms (*15*, *17*, *18*). In the storage region, the single strip had to meet the rolling conditions to ensure that the strip could be wound without exceeding the material's yield condition. This meant that even multistrip configurations could be rolled onto the same hub dimensions without structural failure as long as each individual strip met this rolling condition.

During deployment, rotating the hub unrolled the flat, folded, and rolled FoRoGated-Structure, and the structure entered a shape transition region. This shape transition region connected the storage region, which required a flat folded cross section, to the extension region, which required a corrugated cross section. Both regions had to maintain a consistent cross-sectional shape throughout, not just at the boundaries, leading to both cross-sectional shape boundary conditions and slope boundary conditions at the beginning and end of the shape transition region (*40*). To satisfy these boundary conditions, we inserted two types of shaping components that guided the structure into the desired configurations, as shown in Fig. 2A: folding components that created the flat shape at the start of the transition region and unfolding components that formed the corrugated shape at the end. As depicted in Fig. 2B, serially arranged components ensured that both boundary conditions were satisfied.

After passing the shape transition region, the structure moved into the extension region. To ensure strong mechanical performance in this extended state, it was important to prevent changes in the cross-sectional shape because of the foldable nature of the origami

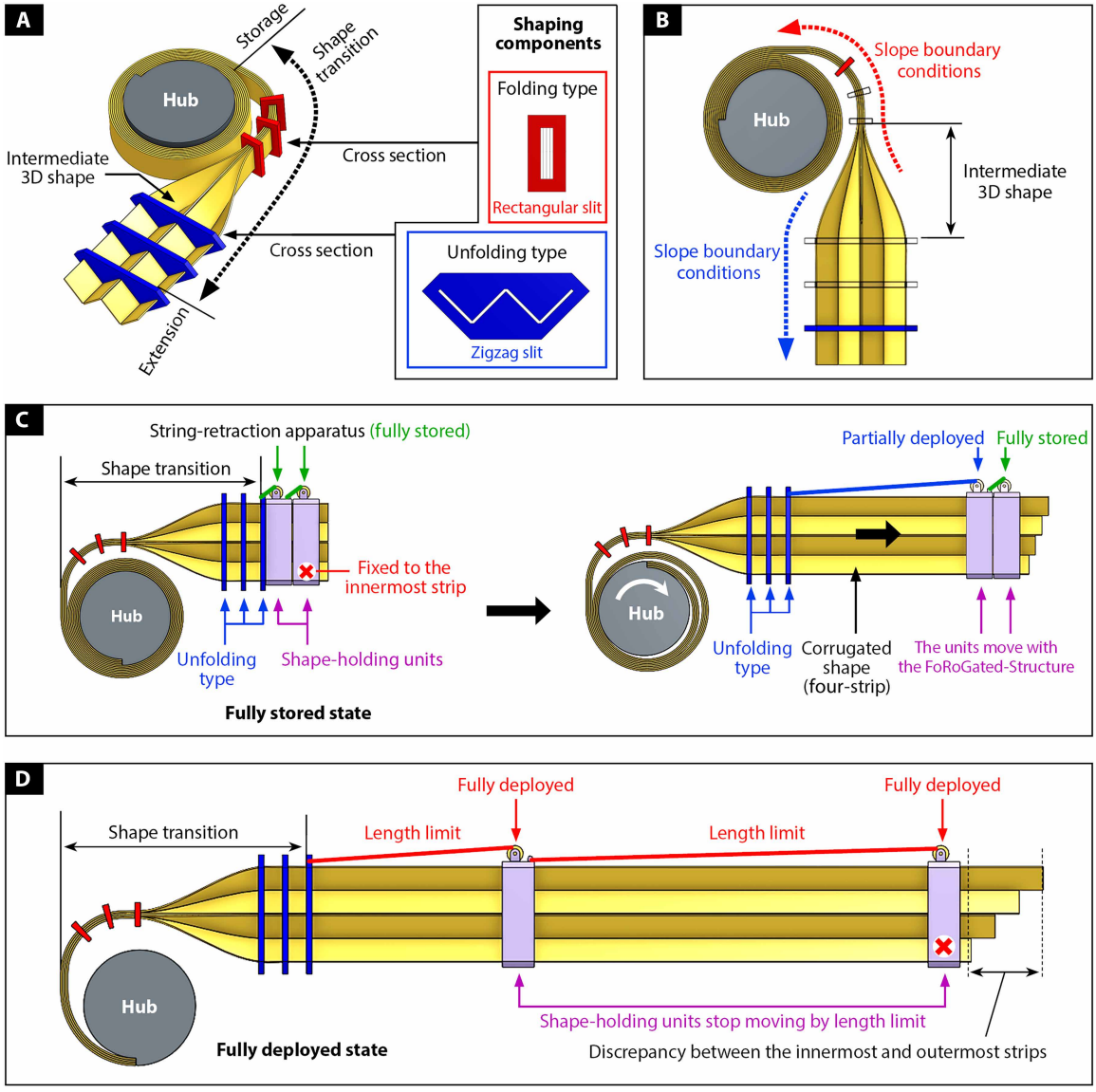


**Fig. 2. Configuration of the extendable mechanism and schematic of the actuation.** (**A**) Overview of the extendable mechanism's three regions and corresponding FoRoGated-Structure shapes. (**B**) Satisfaction of slope boundary conditions by the serial arrangement of shaping components. (**C**) Schematics illustrating the operation process of the mechanism. (**D**) Schematic of the mechanism in the maximum extended state.

structure. Consequently, we inserted shape-holding units at intervals along the deployment length to prevent cross-sectional collapse. Similar to the unfolding components, these units featured target-shaped slits that the FoRoGated-Structure passes through (Fig. 2C). Proper placement of these units ensured the corrugation's robustness by preventing collapse.

To simplify the arrangement of multiple units, we implemented a passive placement method that allowed the units to move without additional actuators during the structure's extension (Fig. 2D). All shape-holding units and the last unfolding component were connected by strings (*41*), which prevented the units from exceeding predetermined intervals. In addition, the final unit was fixed solely to the end of the innermost strip. This configuration allowed the final unit to move along with the extension of the innermost strip while permitting the other strips to slide freely through the slit. As a result, this design effectively accommodated discrepancies between the strips and prevented the structure from falling below its targeted strength. This method also simplified storage by merely reversing the hub's rotation. Consequently, it enabled a simplified, single-motor actuation system for an extendable mechanism.

### Simplified FEM and theoretical models of the FoRoGated-Structure

The mechanical performance of the FoRoGated-Structure in the extended state was a key feature. The complexity of the assembled structure, which combined rigid and flexible materials, posed challenges for achieving precise modeling or an analytical solution. Therefore, we proposed a simplified finite element method (FEM) model and a simplified theoretical model. Although these models might not have fully captured the complex behavior of the actual FoRoGated-Structure, they could be used to approximate the mechanical performance under bending loads, particularly showing greater than 90% accuracy in predicting the critical strength.

First, to achieve an appropriate simplified FEM model, we focused on a real failure mode, where excessive bending loads caused the strip's local buckling between the ribbon's weaving patterns (movie S5). It appeared that adjacent strips constrained each other's movement at the intersections of the ribbon edges ("Observed failure mode in bending" section in the Supplementary Methods). Because this failure mode arose from the unique interlacing characteristic of the FoRoGated-Structure, we developed the simplified FEM model by introducing multiple interlacing points to hold the adjacent strips together, as shown in Fig. 3A. These interlacing points restricted two degrees of freedom in the transverse direction of strips, thereby allowing for controlled sliding, folding, and buckling motion. The distance between these points ($d_r$) could be expressed in terms of the ribbon's width ($w_r$) and thickness ($t_r$) and the strip's width ($w_s$) and thickness ($t_s$) ("Detailed description of the FoRoGated-Structure" section in the Supplementary Methods)

$$d_r = \frac{\left(2w_s + 2t_s + 4t_r\right) w_r}{\sqrt{\left(2w_s + 2t_s + 4t_r\right)^2 - w_r^2}} \tag{1}$$

Second, to construct an appropriate simplified theoretical model, we focused on how the interlacing constrained the deformation of the strips. Figure S1 and movie S6 show a top view of a structure's deformation under the bending moment, where adjacent strips were connected through multiple regularly spaced points. The lines connecting the points remained nearly straight during bending, whereas the edges of the structure without interconnecting points bulged outward. Notably, even during the buckling of the internal strips, the straightness of these lines was preserved, suggesting that the tilt angles of the internal strips at the interlacing points remained constant throughout the bending process.

The observation that points remained in a straight line indicated that the constraints imposed on the internal strip remained unchanged. From this, we inferred that the deformation of the internal strip could be analyzed independently. However, when the edge strip collapsed under severe loading conditions, the interlacing points associated with the edge strip might have shifted from their original positions. This shift altered the boundary conditions of adjacent internal strips, thereby breaking the assumption of their independence. Therefore, we assumed that the internal strips behaved independently only until the edge strips collapsed and triggered changes in the interlacing constraints.

On the basis of these assumptions, we applied a superposition method to decompose the *N*-strip structure, as illustrated in Fig. 3B. The internal strips, which were constrained on both sides, were modeled as a single internal strip multiplied by a factor of $N - 2$. On the other hand, the two edge strips were approximated as a two-strip model. This decomposition reduced the overall analysis to two components: the behavior of the internal strip scaled by $N - 2$ and the behavior of the two edge strips modeled by a two-strip system.

Because the behavior of the internal strip closely resembled lateral-torsional buckling (*42*), it could be simplified using an idealized elastic–perfectly plastic response, characterized by two parameters: the initial stiffness and the critical moment. Under ideal buckling behavior, the cross-sectional shape remained unchanged until the critical moment was reached. The flexural stiffness of a single tilted strip ($EI_\theta$) was expressed on the basis of the tilted angle ($\theta$) and $w_s$ and $t_s$, as follows:

$$EI_\theta = E\frac{w_s^3 t_s}{12}\cos^2\theta \tag{2}$$

When an external bending load ($F_{1,\theta}$) was applied to the tip of the structure of length $L$, lateral buckling was expected to occur at the segment between interlacing points, where the moment was the greatest. The critical moment of a single tilted strip ($M_{1,\theta}$) was expressed as follows (*43*) ("Lateral-torsional buckling criteria for the internal strip" section in the Supplementary Methods):

$$M_{1,\theta} = F_{1,\theta}\, L = \frac{\frac{\pi}{6}}{k(\theta)\, d_r} \frac{E\sqrt{\frac{1}{2(1+\nu)}}\, w_s t_s^3}{\sqrt{\cos^2\theta + \left(\frac{t_s}{w_s}\sin\theta\right)^2}} \tag{3}$$

Here, $\nu$ was the Poisson's ratio of the material and $k(\theta)$ was a characteristic function for the boundary and loading conditions. However, because of the complexity of the ribbon's intertwined boundary conditions, it was difficult to express $k(\theta)$ theoretically. Therefore, $k(\theta)$ was fitted on the basis of the FEM simulation results of the critical moment for each value of $\theta$. The resulting function $k(\theta)$ could be approximated as follows ("Estimation of the characteristic function for deriving the effective length" section in the Supplementary Methods):

$$k(\theta) = 19.2631\theta^3 - 36.3025\theta^2 + 24.2817\theta - 4.5423 \tag{4}$$

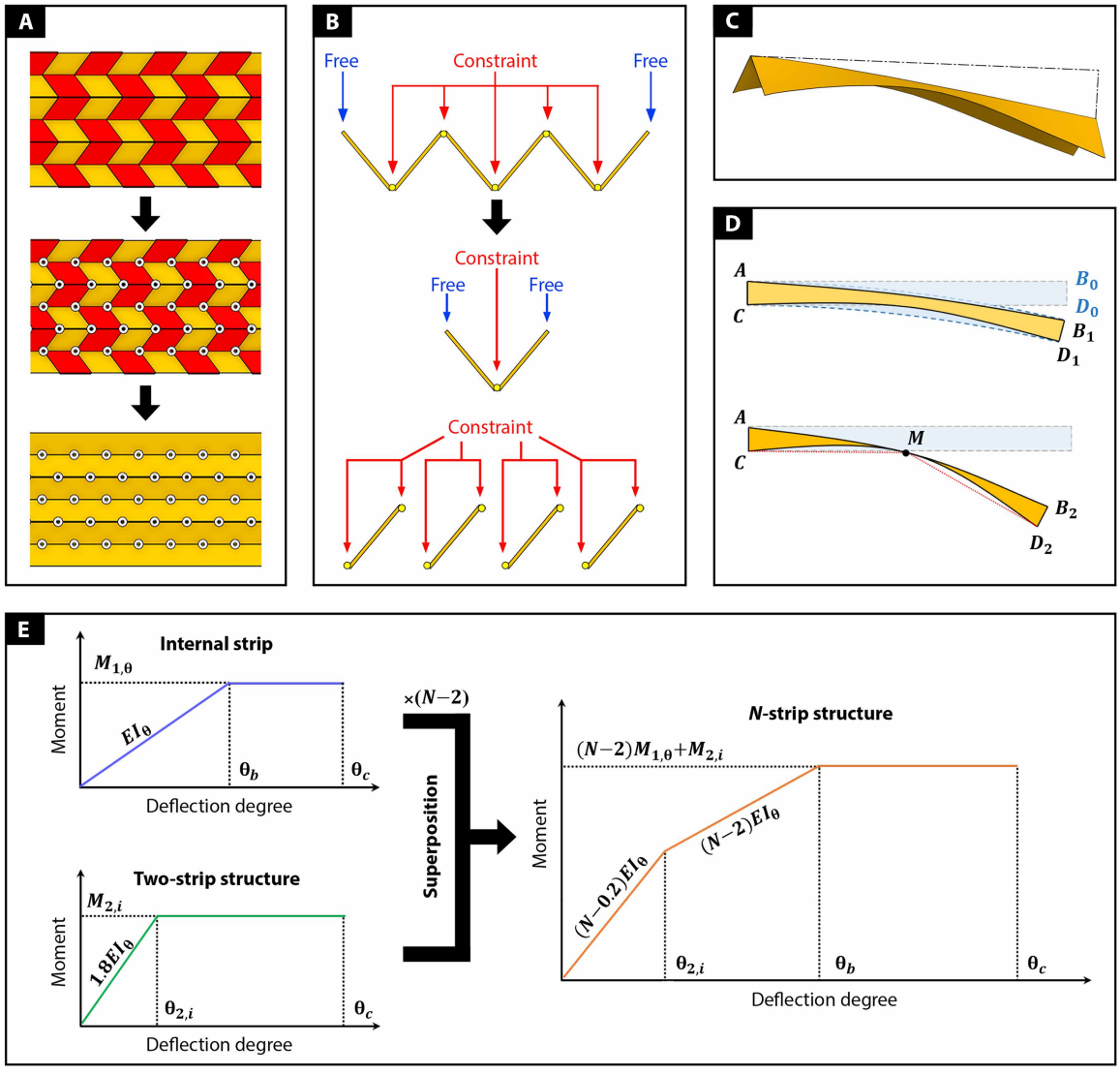


**Fig. 3. FoRoGated-Structure's simplified model for FEM and superposition method.** (**A**) Process of forming the simplified FEM model, involving multiple interlacing points that serve to hold adjacent strips together. (**B**) Process of forming the superposition model. (**C**) The bent two-strip structure under an external load at the tip in the –*X*-directional moment. The cross section is progressively flattening. (**D**) Side view of the two-strip structure undergoing bending through three stages: undeformed (0), intermediate (1), and collapsed (2). (**E**) Schematic illustration of the superposition method.

Using the obtained flexural stiffness and critical moment, we established a first-order elastic–perfectly plastic model for a single internal strip. The deflection angle ($\theta_b$) and distance ($\delta_b$) at buckling, where the linear stiffness curve reached the critical moment, were expressed as follows:

$$\theta_b = \frac{\delta_b}{L} = \frac{F_{1,\theta}L^2}{3\,EI_\theta} = \frac{M_{1,\theta}L}{3\,EI_\theta} \tag{5}$$

Using these relationships, the behavior of a single internal strip could be simplified in an ideal lateral buckling model.

Before simplifying the two-strip model behavior, we first defined the collapse point of the two-strip structure. Figure 3C illustrates the two-strip structure between the shape-holding units under bending, with the load applied at the tip in the –*X* directional moment. When viewed from the side, the deformation of the two-strip structure proceeded through three distinct stages: the undeformed state (0), an intermediate deformed state (1), and the final collapsed state (2), as shown in Fig. 3D. If the cross section exhibited sufficient stiffness, the top curve $AB_1$ and bottom curve $CD_1$ had to exhibit an offset relationship: The top curve underwent elongation, whereas the bottom curve experienced compression, resulting in substantial energy being stored in the structure. However, in a two-strip structure with a deformable cross section, the geometry adjusted to minimize total strain energy, with the top curve undergoing less elongation and the bottom curve experiencing less compression. This caused the two curves to gradually move closer to each other. Eventually, when the two curves, $AB_2$ and $CD_2$ met, they were no longer under elongation or compression, and the structure could no longer store substantial energy. We defined this state as the complete collapse of the edge strips.

Because calculating the exact curved shape was highly complex, we introduced a geometric simplification by defining a midpoint $M$. The straight line connecting point $C$ to point $D_2$ via $M$ had to be less than or equal to the initial length of the structure, as follows:

$$\overline{CM} + \overline{MD_2} \leq \overline{BC_0} = L_d \quad (6)$$

Here, $L_d$ was a distance between the shape-holding units. Consequently, we could obtain the collapse deflection angle ($\theta_c$) and distance ($\delta_c$) using a numerical approach implemented in MATLAB ("Derivation of the minimal deflection angle where the collapse begins" section in the Supplementary Methods)

$$\theta_c = \frac{\delta_c}{L_d} = 2.43\frac{w_s \cos\theta}{L_d} \quad (7)$$

On the basis of the point of collapse, we approximated the behavior of the two-strip model using a first-order elastic–perfectly plastic model. Reflecting the FEM simulation results, we defined the flexural stiffness ($EI_{2,i}$) and critical moment ($M_{2,i}$) of the two-strip model according to the direction $i$. These values were expressed as follows ("Simplification of the 2-Strip FoRoGated-Structure's behavior" section in the Supplementary Methods):

$$EI_{2,+X} = EI_{2,-X} = 0.9\left(2EI_\theta\right),\ EI_{2,Y} = 0.9\left(2EI_{\frac{\pi}{2}-\theta}\right) \quad (8)$$

$$M_{2,+X} = \alpha_{+X}\left(2M_{1,\theta}\right),\ M_{2,-X} = \alpha_{-X}\left(2M_{1,\theta}\right),\ M_{2,Y} = \alpha_Y\left(2M_{1,\frac{\pi}{2}-\theta}\right) \quad (9)$$

Here, $\alpha$ was a dimensionless scaling factor representing the direction-dependent contribution of the two-strip structure. The values of $\alpha_{+X}$, $\alpha_{-X}$, and $\alpha_Y$ were set to 1.00, 0.30, and 0.26, respectively. Last, the simplified theoretical superposition model for the arbitrary $N$-strip FoRoGated-Structure could be expressed as illustrated in Fig. 3E.

The proposed simplified superposition model captured the structural behavior up to the point of edge strip collapse, $\theta_c$. The failure mode could be classified by comparing the critical angle for internal strip buckling, $\theta_b$, and that for $\theta_c$. If internal buckling occurred first ($\theta_b < \theta_c$), the internal strips reached their full load-bearing capacity before the overall structural failure. In contrast, if edge collapse occurred first ($\theta_c < \theta_b$), the flattening of the edge strips could shift the positions of the interlacing points, preventing the internal strips from achieving their full load-bearing performance.

### Comparison between simplified models and experimental results

We conducted a comparison among the results of the theoretical superposition model, the FEM model, and the physical experiments on the actual FoRoGated-Structure. These comparisons were performed under various conditions, including different numbers of strips, loading directions, and distances between shape-holding units. Details for simulation and experimental conditions are provided in the Materials and Methods.

Among the conditions, $L_d$ was determined by considering the sequence of occurrence of internal buckling and edge strip collapse. For the given geometric conditions, internal buckling and edge strip collapse occurred simultaneously ($\theta_b = \theta_c$) when the distance between shape-holding units was 650 mm. Therefore, the 600-mm case (Fig. 4) was selected to represent a scenario where internal buckling slightly preceded edge strip collapse ($\theta_b \leq \theta_c$). Additional results for different distances between shape-holding units were provided in figs. S2 and S3. The 400-mm case (fig. S2) represented a scenario where edge strip collapse was more effectively constrained ($\theta_b \ll \theta_c$), whereas the 800-mm case (fig. S3) represented a scenario where edge strip collapse occurred before internal buckling ($\theta_b > \theta_c$).

First, the results from the FEM model and the superposition model were compared. The FEM model represented idealized, balanced structures with no imperfections, and the superposition model simplified the $N$-strip structure's behavior by using the two-strip structure's FEM results ("Estimation of the characteristic function for deriving the effective length" and "Simplification of the 2-Strip FoRoGated-Structure's behavior" sections in the Supplementary Methods). Despite being derived solely from the two-strip configuration, the superposition model showed good agreement with the FEM results even for the four-strip and six-strip configurations, demonstrating its scalability. With this superposition approach, we were able to reasonably predict key characteristics such as stiffness, critical moment, and bifurcation points. Even for configurations with arbitrary strip angles, strip dimensions, and ribbon spacings, the consistency between the superposition model and FEM results appeared to be secure ("FoRoGated-Structure behavior estimation using the superposition method" section in the Supplementary Methods). This suggested that the superposition model was well suited for rapid estimation of mechanical performance under ideal, defect-free conditions.

In the case of the experiment, the results showed notable differences from the two simplified models. These differences appeared to be mainly caused by imperfections in the real structure, which could reduce stiffness and critical moments (*44*). For stiffness, the experimental values were generally lower than those predicted by the models. However, when the maximum moment of the superposition model was regarded as the critical moment, the experimental results could be classified into two groups depending on the critical moment: one group showing a notably lower value than the model prediction and the other group converging to the model prediction.

To explain this distinction, we classified the structures on the basis of their postbuckling behavior: an unstable type, where stiffness became negative and load-bearing capacity decreased after bifurcation, and a stable type, where stiffness remained positive and load-bearing capacity was sustained or even increased after bifurcation (*45*, *46*). These types could be identified from FEM results through their postbuckling behaviors. Under conditions with geometrical imperfections, the unstable type might have experienced premature snap-through, preventing it from reaching the ideal critical moment. In contrast, for the stable type, geometric imperfections might have lowered prebuckling stiffness but had a negligible effect on the critical moment under bending without eccentricity (*46*). This linked the two types to the experimental groups: the unstable type with results where the load-bearing capacity was lower than the model prediction and the stable type with results where the load-bearing capacity converged to the model prediction. Consequently, classifying the type in advance using FEM enabled the prediction of how the structure would behave in real-world conditions, and for the stable type, the actual critical moment could be estimated using the simplified superposition model.

On the basis of this stable-unstable classification, the FoRoGated-Structure was analyzed as follows. From the FEM results for the

600-mm case ($\theta_b \leq \theta_c$) in Fig. 4, bending in the $\pm X$-directional moment cases showed stable behavior from the four-strip configuration onward, and bending in the $Y$-directional moment cases showed stable behavior from the six-strip configuration. Comparing these results with other cases (figs. S2 and S3), several trends were observed: Bending in the $+X$-directional moment cases tended to be the most stable, whereas the $Y$-directional cases tended to be the least stable; increasing the number of strips and decreasing the spacing between shape-holding units tended to enhance stable behavior. These trends seemed to be attributed to more effectively constrained internal strip boundaries and suppression of edge collapse.

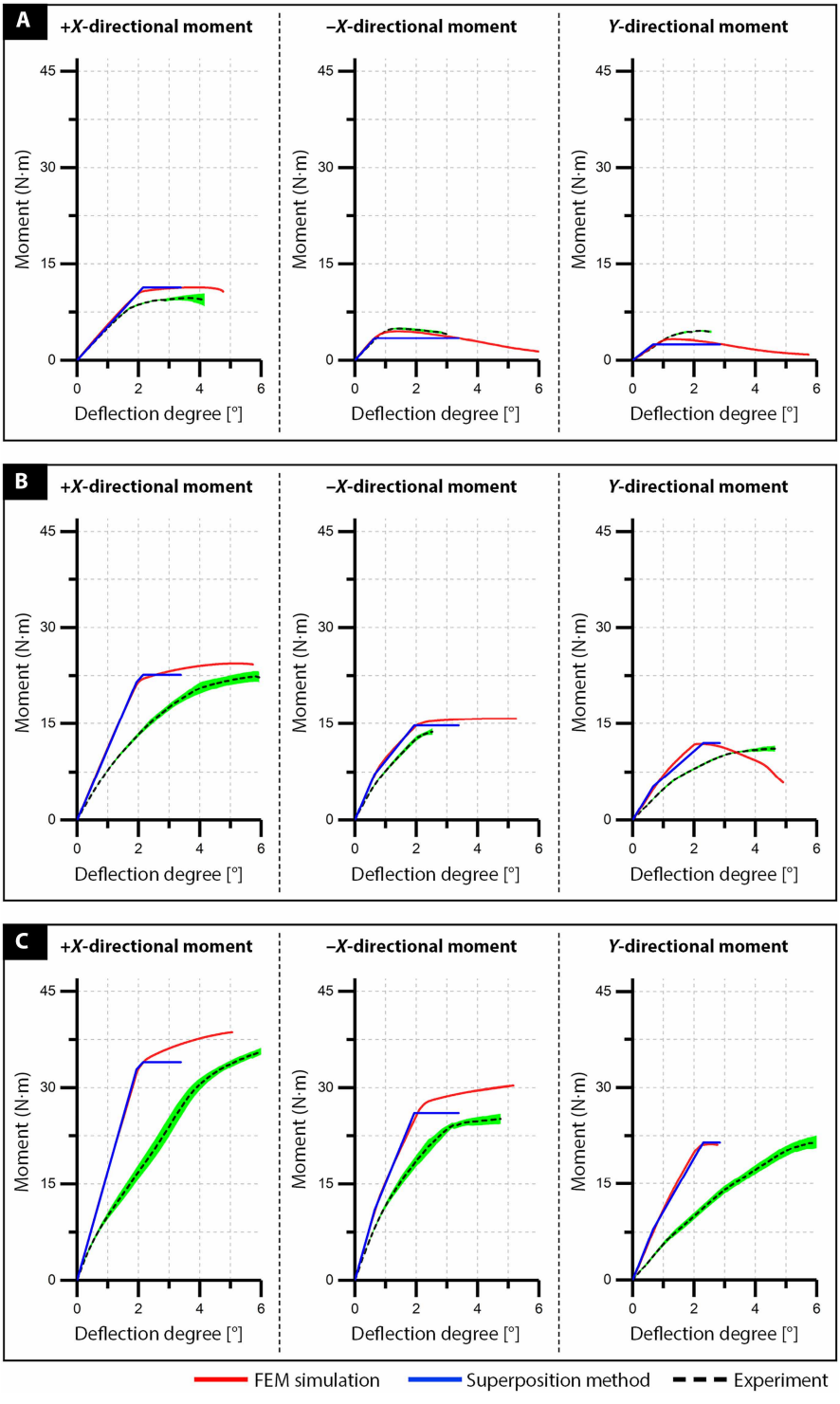


**Fig. 4. FEM simulation, superposition model, and experimental results for the 600-mm specimen ($\theta_b < \theta_c$).** (**A**) Two-strip FoRoGated-Structure. (**B**) Four-strip FoRoGated-Structure. (**C**) Six-strip FoRoGated-Structure. [(A) to (C)] Red line: FEM simulation; blue line: superposition model; black dashed line: experimental mean ($n = 3$); light green band: experimental variability, ±1 SD ($n = 3$).

One additional point was that although increasing the number of strips tended to promote stability, the stiffness discrepancy between experiments and models became more pronounced. The increase in strip number was likely to have caused difficulty in achieving perfect alignment of all strips with the target geometry, resulting in a decrease in stiffness. Furthermore, as illustrated in fig. S4, the steel strips used in the FoRoGated-Structure exhibited slight in-plane curvature. These precurved geometries inevitably introduced cross-sectional distortions, resulting in additional geometric imperfections.

In summary, although imperfections generally reduced stiffness relative to the FEM and superposition models, the proposed superposition method still provided reliable predictions of the critical moment for stable cases. Although FEM simulations offered the most rigorous means of identifying whether the structure exhibited stable or unstable behavior, configurations with four or more strips could be regarded as stable under $X$-directional moment loading when internal buckling occurred at or before edge strip collapse ($\theta_b \leq \theta_c$). Furthermore, if geometric imperfections could have been effectively controlled and appropriate weighting factors introduced to compensate for them, the superposition method could have been extended to provide accurate stiffness predictions as well.

## Comparison with the conventional rollable structures

In the case of thin-walled rollable structures such as the STEM and the TRAC boom, the height-to-radius ratio of the hub was fixed to achieve maximum performance, meaning that all design parameters were governed by a single variable ("Relations between the achievable stiffness and the hub dimension" section in the Supplementary Methods). The STEM boom featured a relatively narrow and tall hub, whereas the TRAC boom used a shorter and wider hub configuration. When the hub height was matched, the TRAC boom achieved more than 30 times the stiffness of the STEM boom but required a hub radius of ~7.6 times larger. However, if the TRAC boom sacrificed its optimal geometry to match both the hub height and radius of the STEM boom, its stiffness advantage was reduced to ~3.8 times that of the STEM boom.

Unlike conventional structures, the FoRoGated-Structure featured multiple independent design variables. The directional flexural stiffness of the $N$-strip FoRoGated-Structure ($EI_{XX,N}$, $EI_{YY,N}$) could be adjusted through various independent parameters, as expressed below

$$EI_{XX,N} = E(N-0.2)\left(\frac{R_h}{H_h}\right)\frac{\cos^2\theta}{6}\varepsilon_y H_h^4 \tag{10}$$

$$EI_{YY,N} = E(N-0.2)\left(\frac{R_h}{H_h}\right)\frac{\sin^2\theta}{6}\varepsilon_y H_h^4 \tag{11}$$

Here, $R_h$ and $H_h$ were the radius and height of the hub, respectively, and $\varepsilon_y$ was the allowable yield strain. In terms of structural strength, assuming that the spacing between shape-holding units was sufficiently short to suppress edge strip collapse, the directional critical moment of the $N$-strip FoRoGated-Structure ($M_{N,+X}$, $M_{N,-X}$, and $M_{N,Y}$) could be expressed as follows

$$M_{N,+X} = N\frac{\left(\frac{4\pi}{3}E\sqrt{\frac{1}{2(1+\nu)}}\right)\frac{(\varepsilon_y R_h)^3 H_h}{k(\theta)d_r}}{\sqrt{\cos^2\theta + \left(\frac{2\varepsilon_y R_h}{H_h}\sin\theta\right)^2}} \tag{12}$$

$$M_{N,-X} = (N-1.4)\frac{\left(\frac{4\pi}{3}E\sqrt{\frac{1}{2(1+\nu)}}\right)\frac{(\varepsilon_y R_h)^3 H_h}{k(\theta)d_r}}{\sqrt{\cos^2\theta + \left(\frac{2\varepsilon_y R_h}{H_h}\sin\theta\right)^2}} \tag{13}$$

$$M_{N,Y} = (N-1.48)\frac{\left(\frac{4\pi}{3}E\sqrt{\frac{1}{2(1+\nu)}}\right)\frac{(\varepsilon_y R_h)^3 H_h}{k\left(\frac{\pi}{2}-\theta\right)d_r}}{\sqrt{\sin^2\theta + \left(\frac{2\varepsilon_y R_h}{H_h}\cos\theta\right)^2}} \tag{14}$$

The presence of multiple independent design variables not only enabled geometric flexibility in hub design but also allowed the structure to achieve high stiffness and strength, even when one of the design parameters was constrained. For example, when the hub height was limited but high stiffness was required, the stiffness could be enhanced by enlarging the hub radius or increasing the number of strips. Moreover, the linear increase in stiffness and strength with the number of strips highlighted the scalability of the FoRoGated-Structure in terms of mechanical performance.

Table 1 compares the performance of the FoRoGated-Structure with that of the TRAC boom (*19*), a representative conventional rollable structure known for its high bending stiffness. In this comparison, both structures were assumed to have the same hub height and radius and were made of the same material. The material used for the TRAC boom (*19*) was presumed to have a Young's modulus of 100 GPa and an allowable strain of 1.5%. The FoRoGated-Structure, for comparison, was configured with strips of 24.6 mm in width and 0.816 mm in thickness and arranged at an angle of 40°, with a spacing of 28 mm between the interlacing points. Its mechanical properties were derived on the basis of the equations introduced earlier. The values in parentheses in Table 1 indicate the ratio of the performance of the FoRoGated-Structure to that of the TRAC boom.

As shown in Table 1, the FoRoGated-Structure exhibited distinct scaling with the number of strips. Bending stiffness increased approximately linearly with the number of strips across directions, as expected from the second moment of area of the undeformed cross section. When compared with TRAC, the stiffness of the $N$-strip FoRoGated-Structure was slightly less than $N$ times that of the TRAC boom. On the other hand, for the critical moment, the increase was governed by the number of internal strips. With two strips and no internal strips present, the $+X$-directional critical moment was much larger than those of the $-X$ and $Y$ directions, revealing a directional imbalance. This tendency was also observed in the TRAC boom. As the strip count increased and internal strips were introduced, these internal strips began to carry substantial load even in $-X$ and $Y$ directions. Consequently, whereas the $+X$ critical moment continued to increase roughly linearly with the number of strips, from four strips onward, the $-X$ and $Y$ capacities rose sharply and exceeded those of the TRAC boom by a wide margin. This indicated that directional strength became substantially more uniform as the number of strips increased: The TRAC boom's $Y$-directional critical moment was about 30% of its primary direction value, whereas the FoRoGated-Structure reached about 54% with four strips and about 64% with six strips.

On the other hand, the two structures were also compared considering their weight. The TRAC boom structure was composed of two overlapping layers, where each layer was 0.408 mm thick, resulting in a total thickness of 0.816 mm. The $N$-strip FoRoGated-Structure was composed of $N$ individual strips, each with a thickness of 0.816 mm. This suggested that the $N$-strip FoRoGated-Structure with the same hub radius and height used $N$ times the amount of material used in the TRAC boom. However, in terms of stiffness, the FoRoGated-Structure did not achieve $N$ times the stiffness of the TRAC boom. This resulted in the FoRoGated-Structure having a slightly lower stiffness-to-weight ratio, at ~80% of that of the TRAC boom. Nevertheless, in terms of the strength-to-weight ratio along the $+X$ axis, the FoRoGated-Structure performed ~150% compared with the TRAC boom. Along the $Y$ axis, its strength-to-weight ratio exceeded that of the TRAC boom by at least 250% from the four-strip configuration onward. This suggested that the FoRoGated-Structure provided a structurally tougher design.

In comparison with conventional rollable structures, the FoRoGated-Structure exhibited lower storage efficiency. The storable space of a rollable structure was defined as the volume of the storage region excluding the portion occupied by the hub, and conventional designs, typically made from a single material, could fill most of this space densely with their main structural material. In the case of the FoRoGated-Structure, however, extra volume was needed to store the flexible ribbons in addition to the main strips. As a result, when storing the same amount of material, the FoRoGated-Structure required more storable space than a conventional rollable structure. The required storage region's radius ($R_{storage}$) for the $N$-strip FoRoGated-Structure of length $L$ could be calculated as follows ("Detailed descriptions of the FoRoGated-Structure's storage" section in the Supplementary Methods):

$$R_{storage} = Nt_s\left(1+\frac{3}{2}\frac{t_r}{t_s}\right) + \sqrt{\frac{1.25}{\pi}Nt_s\left(1+\frac{3}{2}\frac{t_r}{t_s}\right)L + R_h^2} \tag{15}$$

**Table 1. Flexural stiffness and critical moment comparison between the TRAC boom and FoRoGated-Structure for the same hub dimensions.** For both, $R_h$ = 27.2 mm (ε = 1.5%) and $H_h$ = 24.6 mm. M. dir., moment direction.

| Type | $t_{roll}$ \| $t_{flat}$ [mm] | M. dir. | Flexural stiffness [N·m$^2$] ($EI/EI_{TRAC}$) | Critical movement [N·m] ($M/M_{TRAC}$) |
|---|---|---|---|---|
| TRAC (*19*) | 0.816 \| 0.408 | +*X* | 69 (1) | 10.5 (1) |
| | | –*X* | | 5.64 (1) |
| | | *Y* | 41.4 (1) | 3.17 (1) |
| Two-strip FoRoGated-Structure | 0.816 \| 0.816 | +*X* | 106.9 (1.55) | 31.8 (3.03) |
| | | –*X* | | 9.55 (1.69) |
| | | *Y* | 75.3 (1.82) | 6.95 (2.19) |
| Four-strip FoRoGated-Structure | | +*X* | 225.7 (3.27) | 63.7 (6.07) |
| | | –*X* | | 41.4 (7.34) |
| | | *Y* | 158.9 (3.84) | 33.7 (10.63) |
| Six-strip FoRoGated-Structure | | +*X* | 344.5 (4.99) | 95.5 (9.10) |
| | | –*X* | | 73.2 (12.98) |
| | | *Y* | 242.6 (5.86) | 60.4 (19.05) |

where $t_r$ and $t_s$ are the thickness of the ribbon and strip, respectively.

In summary, the FoRoGated-Structure presented an additional design option in the domain of rollable structures. Although conventional structures might have been more suitable for applications where maximizing the stiffness-to-weight ratio and storage efficiency was the highest priority, the FoRoGated-Structure offered greater design flexibility, making it particularly advantageous for robotic applications that required high load-bearing capacity in all directions—such as supporting a heavy object at the tip. As such, the FoRoGated-Structure had the potential to inspire further advancements in deployable structural systems and to find broad applications across diverse fields.

## Applications to deployable robotic systems

To demonstrate the practical potential of the FoRoGated-Structure, we built two mobile robotic systems. The first used a single structure as a cantilevered robotic arm, and the second used multiple structures to form a deployable frame.

First, we aimed to demonstrate a compact, low-profile mobile robot, which was similar in form to a robotic vacuum cleaner, capable of reaching and manipulating objects on shelves in a wide operational workspace (Fig. 5A). To achieve a thin form factor, the height of the hub storing the rollable structure also had to be minimized. As a result, we fabricated a four-strip FoRoGated-Structure using four steel strips, each 0.5 mm thick and 19 mm wide. The fabricated structure could be wound into a hub with a 50-mm radius and 19-mm height while sustaining a strain of 0.5%. This structure's flexural stiffness was approximately eight times higher than that of the TRAC boom, when both were designed with the same hub dimensions and made from the same material ("Relations between the achievable stiffness and the hub dimension" section in the Supplementary Methods). If the spacing between shape-holding units was less than 650 mm, its predicted critical moment was 22.63 N·m in the +*X* direction.

To enable shelving tasks, the structure must extend to approximately human height. Consequently, the storage region was designed with a radius of 77.5 mm, allowing it to accommodate a FoRoGated-Structure up to 1600 mm in length (Fig. 5B). As a result, the mechanism extended the arm from 386 to 1936 mm (502%), as shown in Fig. 5C and movie S7. The mechanism was designed with shorter spacing between shape-holding units near the base and larger spacing toward the tip, because this shorter spacing did not enhance the ideal ultimate strength but could mitigate unpredictable imperfections under real loading conditions. Given that the moment induced by self-weight was ~7.81 N·m ("Equivalent moment load from self-weight in the cantilevered robotic arm" section in the Supplementary Methods), the ultimate tip load in the fully extended, horizontal state was estimated to be 0.9 kg. In practice, it extended horizontally while supporting a 0.5-kg payload with a safety factor of 1.8 (Fig. 5D and movie S8). As shown in Fig. 5E and movie S9, this robot handled objects on shelves and pressed elevator buttons, offering an expansive range of operations.

For the other application, we presented the concept of a deployable, meter-scale mobile gantry robotic system to demonstrate that the proposed rollable structure could be applied not only to small-scale systems but also to large-scale systems. As illustrated in Fig. 6A, the system consisted of three components: a tetrahedral deployable gantry frame constructed from three extendable mechanisms, a cable-driven parallel robot (CDPR) mounted on top of the frame, and three mobile robots positioned beneath each extendable mechanism to provide both mobility and deployment functionality ("Detailed description of the mobile robot" section in the Supplementary Methods). The targeted deployed tetrahedral frame, consisting of three mechanisms that were extended to about 3.75 m at an angle of ~62.5° from the ground, must be structurally robust enough to support the CDPR system during and after deployment. To demonstrate that the deployable frame had mechanical properties sufficient to support CDPR operations, we aimed to carry out a 3D-printing task using the gantry robotic system, because this task demanded repeatability to successfully stack the next layers.

The CDPR system used in this system was developed on the basis of the open-source Hangprinter project (*47*, *48*) and weighed ~12.5 kg, including a 2-kg end effector that extruded polylactic acid (PLA) filament through a 1.2-mm nozzle ["Detailed description of

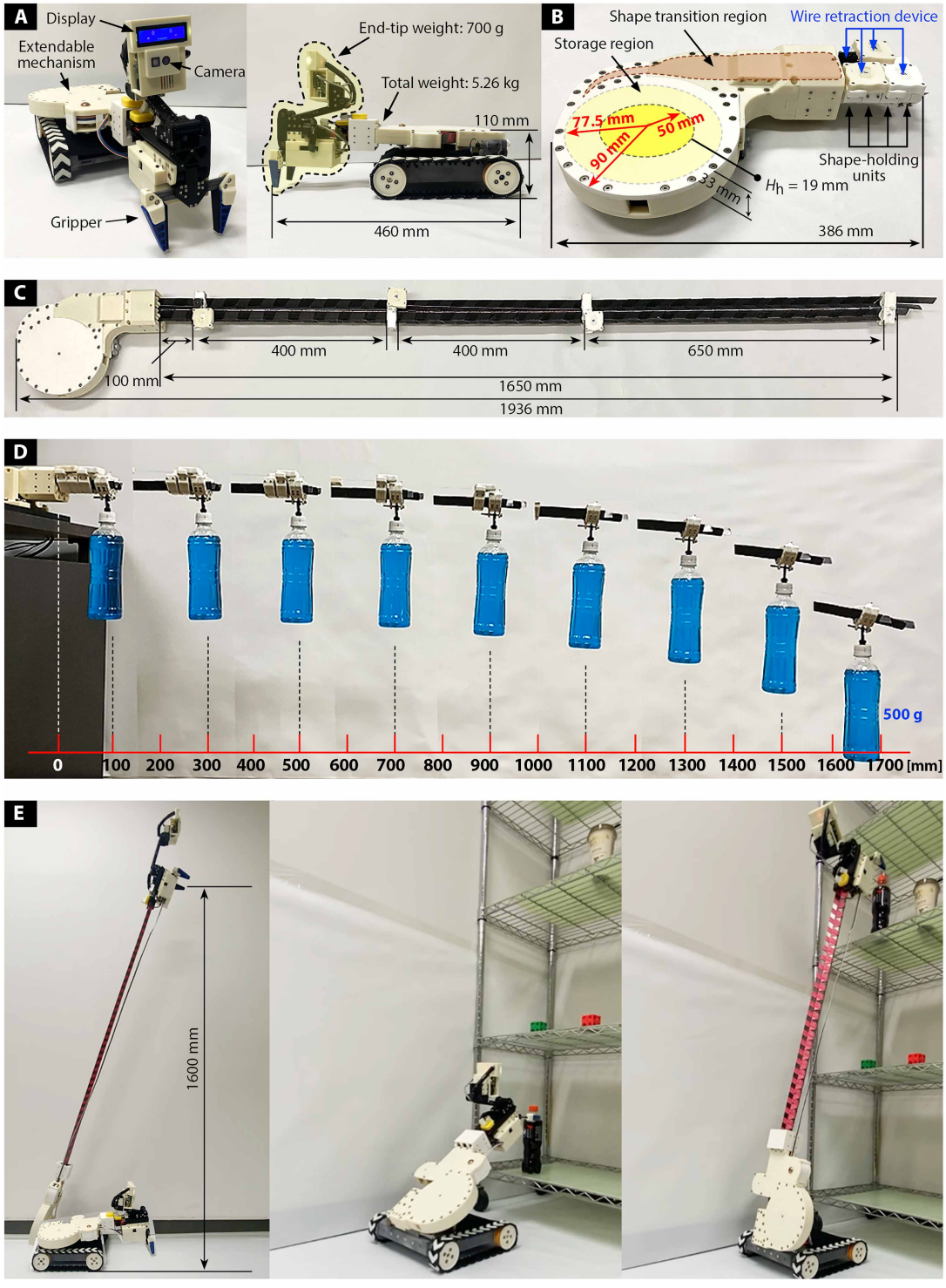


**Fig. 5. A compact mobile robot capable of reaching and manipulating objects on shelves.** (**A**) Fabricated robotic-vacuum–sized mobile robot, equipped with the extendable mechanism, a gripper, and a camera. (**B**) Detailed components and size of the extendable mechanism. (**C**) The extendable mechanism's fully extended state. (**D**) The extendable mechanism can extend horizontally while supporting a 500-g payload. (**E**) The robotic-vacuum–sized mobile robot can reach up to 1600 mm in height and handle objects on shelves, offering an expansive range of operations.

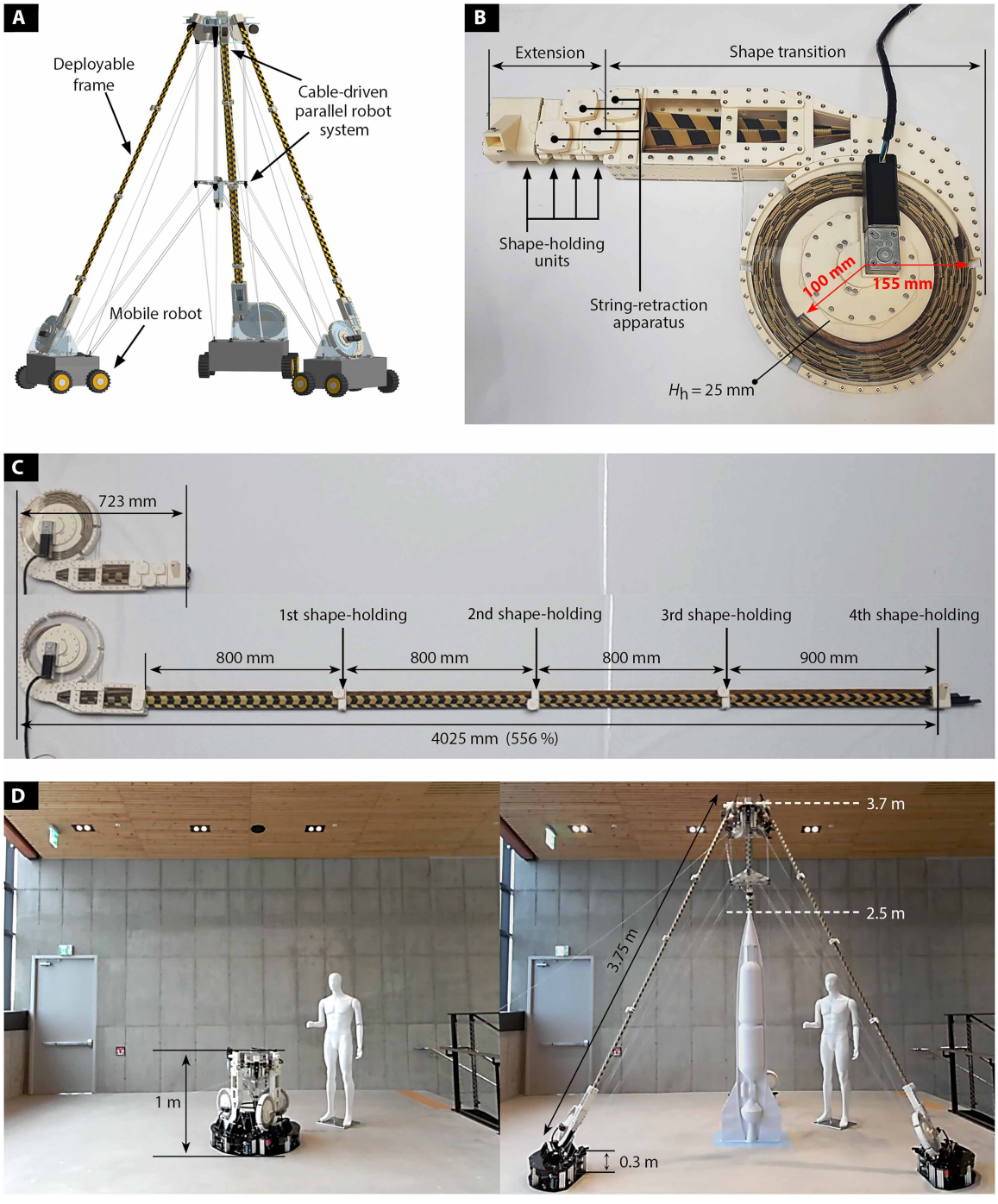


**Fig. 6. Meter-scale deployable 3D-printing mobile robotic system.** (**A**) Conceptual illustration of the deployable mobile 3D-printing robotic system. (**B**) Detailed components and size of the extendable mechanism. (**C**) The extendable mechanism's fully stored state and extended state. (**D**) A fabricated meter-scale deployable mobile robotic system for 3D printing. The system transforms a 0.7-m-high triangular column into a 3.4-m-high tetrahedral frame and successfully constructs a 2.5-m-tall structure.

the 3D-printing cable-driven parallel robot (CDPR)" section in the Supplementary Methods]. To support the 12.5-kg CDPR system in the target tetrahedral frame, each extended mechanism must be able to withstand at least 4.17 kg when extended to 3.75 m at 62.5° from the ground. To enhance the load-bearing capacity of the rollable structure, we fabricated a FoRoGated-Structure using four steel strips, each 1 mm thick and 25 mm wide, which were wider and thicker than earlier prototypes. The structure could be rolled into a hub with a radius of 100 mm and a height of 25 mm, while sustaining only 0.5% strain. Table 2 provides a summary of the directional stiffness and strength of the structure predicted by the superposition model, depending on the spacing between the shape-holding units.

**Table 2. Directional flexural stiffness and critical moment of the four-strip FoRoGated-Structure predicted by the superposition model, depending on the spacing between the shape-holding units.**

| | Flexural stiffness (N·m$^2$) | Critical moment depending on spacing (N·m) | | |
|---|---|---|---|---|
| | | 1000 mm | 800 mm | 600 mm |
| +*X*-directional bending moment | 580.7 | 81.2 | 126.9 | 225.5 |
| –*X*-directional bending moment | | 78.5 | 102.5 | 154.42 |
| *Y*-directional bending moment | 408.9 | 48.0 | 65.4 | 96.1 |

To achieve a 3.75-m extension, we fabricated the extendable mechanism, as shown in Fig. 6B. The storage region was designed with a radius of 155 mm, allowing it to accommodate a FoRoGated-Structure up to 3370 mm in length. The prototype successfully demonstrated the storage of a 3300-mm-long structure, enabling an extension from 723 to 4025 mm (556%), as shown in Fig. 6C and movie S10. When deployed into the 3.75-m length, the length of the extruded FoRoGated-Structure was ~3 m. For a 3-m-long structure deployed at a 62.5° angle to withstand at least 4.17 kg, the minimum required moment capacity was 112 N·m with a safety factor of 1.8, similar to the previous application. Consequently, the spacing between shape-holding units was selected to be 800 mm.

As shown in movie S11, the system successfully completed an operational scenario, including movement to target locations, deployment, 3D printing of a target structure, and withdrawal ("Detailed system operation" section in the Supplementary Methods). During deployment, the frame expanded from a compact triangular column (side of the equilateral triangle: 420 mm, height: 730 mm) to a large tetrahedral frame (side of the equilateral triangle: 3200 mm, height: 3430 mm) while supporting the 12.5-kg CDPR-mounted tip. Once deployed, the CDPR operated the 2-kg end effector by controlling four cables routed to the frame's vertices. Equipped with a 1.2-mm nozzle, the end effector extruded PLA material for 3D-printing tasks, maintaining a repeatability error within ±0.6 mm. This precision allowed for the successful construction of a 2.5-m-tall structure composed of 4170 layers (Fig. 6D and movie S12).

The deployable robotic systems using the FoRoGated-Structure demonstrated a successful transition from a compact form to a large operational form, effectively addressing spatial limitations and enhancing the systems' versatility. They had the capacity to support substantial payloads, operate across a broad workspace, and maintain repeatability. These results underscored the potential of the FoRoGated-Structure in enhancing the functionality and applicability of deployable robotic systems in practical scenarios.

## DISCUSSION

To achieve both high rigidity and compact storage, we developed the ribbon-woven interlaced origami design, which offers strong mutual constraints for structural stability and ensures flexibility for fold-and-roll packaging. It also allows for straightforward expansion through simple sewn connections, enhancing structural stiffness and strength without sacrificing flexibility. Moreover, it is possible to fabricate the structure using ready-made strips and ribbons without complex manufacturing processes. Hence, the scalability in structural properties and material can offer a flexible solution for various requirements.

When designing the rollable structure to fit within the same hub dimensions, we demonstrated that the FoRoGated-Structure can achieve enhanced mechanical properties compared with conventional rollable structures. However, the FoRoGated-Structure is a more intricately assembled structure compared with conventional designs and requires additional storage space to accommodate flexible materials such as ribbons. Moreover, the FoRoGated-Structure requires additional shape-holding units for restoring and maintaining the targeted cross-sectional shape, unlike conventional rollable structures. As a result, in applications where structural simplicity is required because of the strict spatial constraints or where maximizing the stiffness-to-weight ratio and storage efficiency is prioritized over absolute stiffness and strength, conventional rollable structures are still more advantageous. Nonetheless, in cases where a low-profile but wide storage region is acceptable, or where achieving extremely high stiffness and strength is prioritized over the stiffness-to-weight ratio and storage efficiency, the FoRoGated-Structure can be a viable alternative.

The actuation of the FoRoGated-Structure requires sufficient hub torque to overcome three primary resistance sources: friction between the ribbon and slipping strips, friction and deformation as the structure passes through the shaping components, and friction as the structure moves through the shape-holding units. These forces primarily act in the shape transition and extension regions. As a result, the torque from the hub is transmitted through the structures in the storage region to the shape transition and extension regions. This causes the structure located in the storage region to experience compressive force during the extension process, whereas it is subjected to tensile force during the storage process. This compressive force can impose a limit on the deployment speed. If excessive torque is applied to achieve rapid deployment, the FoRoGated-Structure within the storage region may buckle, resulting in internal kinking and jamming of the structure. Thus, the maximum torque can be determined by the resistance forces and the stored structure's buckling criteria. Notably, the resistance forces vary depending on factors such as manufacturing precision, component tolerances, and the quality of assembly. Consequently, the actuation performance is highly dependent on the specific configuration and quality of the actuation system. Although this study acknowledges these effects, detailed relationships were not fully analyzed in this work.

We also developed a small-scale FoRoGated-Structure prototype composed of four strips, each 6 mm wide and 0.1 mm thick ("Small-scale FoRoGated-Structure and extendable mechanism"

section in the Supplementary Methods). In this configuration, it was possible to retract the structure by rotating the hub; however, extension failed because of buckling of the stored structure. This failure seems to be attributed to two factors: First, increased frictional resistance caused by simplified components necessitated by the challenges of small-scale fabrication; second, reduced buckling strength exhibited by the FoRoGated-Structure. To address this buckling issue, we introduced an auxiliary mechanism at the boundary between the storage and shape transition regions, which applies additional pushing force to assist the structure in passing through the transition region. This intervention enabled successful deployment without buckling. These findings suggest that although the FoRoGated-Structure is structurally scalable in principle, it may be less advantageous at smaller scales compared with other extendable mechanisms because of the inherent difficulties of miniaturizing structural and actuation components.

In summary, we propose a rollable structure design that combines compact storage with high load-bearing capacity, offering an additional option within the space of rollable structures. Our work has introduced a fold-and-roll interlaced origami design, validated its feasibility through modeling and experiments, and demonstrated its potential in deployable robotic systems. This approach highlights both the structural advantages and practical limitations compared with conventional rollable structures. Although deeper investigations into aspects such as load capacity optimization, imperfection sensitivity, actuation speed, and multifunctional integration were beyond the scope of this initial study, these remain important directions that can build on the present foundation. We anticipate that the FoRoGated-Structure will provide a useful basis for further exploration and inspire advanced developments in deployable structural systems across diverse application fields.

## MATERIALS AND METHODS

### Detailed description of the fabrication method

To fabricate the FoRoGated-Structure, we used a webbing ribbon, steel (ASTM A1008) strips, 0.08-mm-thick Teflon tape (Nitto 903), and 0.32-mm-diameter Dyneema thread for sewing. The Teflon tape was attached to both sides of the steel strips to reduce friction and facilitate smooth sliding. The fabrication process (fig. S5) proceeded in order. In the first step, we applied Teflon tape to both sides of the steel strips to facilitate smooth sliding. In the second step, we wove a ribbon around two strips to form a two-strip unit. In the third step, we repeated the first and second steps to create additional two-strip units. In the fourth step, we aligned the woven patterns of two two-strip units and sewed them together with Dyneema thread. In the fifth step, we continued adding and sewing two-strip units until the desired multistrip structure was obtained. In the final step, we attached the ribbon to the outermost strip to preserve the woven pattern.

The material and dimensions of the ribbon and steel strips could be adjusted according to design requirements. However, when in-plane shear deformation occurred in the ribbon because of shear forces, the length of the loops formed by the ribbon was reduced. To mitigate such deformation in fabric-based ribbons, impregnating and drying the ribbon with a polymer liquid, such as varnish, helped preserve the in-plane geometry.

The FoRoGated-Structure used as the cantilevered robotic arm for the low-profile mobile robot was constructed with 0.45-mm-thick, 23-mm-wide polypropylene (PP) webbing ribbons and 0.5-mm-thick, 19-mm-wide steel strips. The FoRoGated-Structure used for the mobile gantry frame used 0.65-mm-thick, 25-mm-wide Kevlar ribbons and 1-mm-thick, 25-mm-wide steel strips. The structural density for each configuration was 364 g/m and 869 g/m, respectively.

### Experimental and simulation conditions

The bending performance of the FoRoGated-Structure was analyzed by controlling three main parameters: the number of strips, specimen length, and loading direction. A total of 27 cases were examined, covering configurations with two, four, and six strips; specimen lengths of 400, 600, and 800 mm; and bending moment along the $+X$ axis (gravity direction), $-X$ axis, and $Y$ axis. For testing, 0.45-mm-thick, 23-mm-wide PP webbing ribbons ["Tensile test of polypropylene (PP) webbing ribbons" section in the Supplementary Methods] and 0.5-mm-thick, 19-mm-wide steel strips (ASTM A1008) were used. All results are presented in terms of applied torque and resulting deflection angle.

To measure rigidity, we used a universal testing system (Instron 5948 microtester equipped with an Instron 2580-107 2-kN load cell). The experimental setup, shown in fig. S6, consisted of a linear stage and two jigs (stage jig and load-cell jig). The stage jig secured all strips of the FoRoGated-Structure in position on the linear stage, preserving the corrugated cross-sectional shape. The load-cell jig, which clamped one side strip while allowing the other strips to slide, was attached to the load cell. The load-cell jig also included a sliding joint and a rotational joint to accommodate horizontal shrinkage and directional adjustments. Other degrees of freedom at the tip were restricted. The load cell moved at 3 mm/s until the peak force was reached, and three specimens were tested for each case.

For the bending simulation, finite element analysis was conducted using Abaqus (Dassault Systems). Because the Young's modulus of ASTM A1008 is known to be 190 to 210 GPa, a linear elastic model with a modulus of 200 GPa was applied in the simulation. The boundary conditions were set to match the experimental roles of the stage jig and load-cell jig. The loading condition applied uniform displacement at each end of the strips, as shown in fig. S7.

### Statistical analysis

Bending performance was evaluated across 27 cases defined by strip count (two, four, or six), specimen length (400, 600, or 800 mm), and loading direction ($+X$, $-X$, or $Y$). For each case, three specimens ($n = 3$) were tested using the custom jig. To reduce noise, the raw data were smoothed with a moving-average filter via the movmean function in MATLAB (window size = 10). To enable comparison across specimen lengths, force was converted to torque by multiplying by the specimen length, and tip deflection was converted to a deflection angle by dividing by the specimen length. For each case, the sample mean and sample standard deviation (SD) were computed from the three specimens. In Fig. 4 and figs. S2 and S3, the mean is shown as a black dashed curve, and variability is depicted as a light green band corresponding to $\pm 1$ SD ($n = 3$).

## Supplementary Materials

**The PDF file includes:**

Supplementary Methods
Figs. S1 to S31
Table S1
Legends for movies S1 to S12
References (*49*, *50*)

**Other Supplementary Material for this manuscript includes the following:**
Movies S1 to S12

## REFERENCES AND NOTES


1. L. Puig, A. Barton, N. Rando, A review on large deployable structures for astrophysics missions. *Acta Astronaut.* **67**, 12–26 (2010).
2. S. Teshigawara, H. H. Asada, "A mobile extendable robot arm: Singularity analysis and design" in *2019 IEEE/RSJ International Conference on Intelligent Robots and Systems (IROS)* (IEEE, 2019), pp. 5131–5138.
3. J. Kim, J. Bae, Self-locking pneumatic actuators formed from origami shape-morphing sheets. *Soft Robot.* **11**, 32–42 (2024).
4. M. Park, Deployable soft origami modular robotic arm with variable stiffness using facet buckling. *IEEE Robot. Autom. Lett.* **8**, 864–871 (2023).
5. C. C. Kemp, A. Edsinger, H. M. Clever, B. Matulevich, "The design of stretch: A compact, lightweight mobile manipulator for indoor human environments" in *2022 International Conference on Robotics and Automation (ICRA)* (IEEE, 2022), pp. 3150–3157.
6. J. Li, R. Liu, L. Zhang, S. Zuo, H. Wang, "Configuration synthesis and design of a telescopic service robot" in *2018 International Conference on Virtual Reality and Intelligent Systems (ICVRIS)* (IEEE, 2018), pp. 442–445.
7. E. W. Hawkes, L. H. Blumenschein, J. D. Greer, A. M. Okamura, A soft robot that navigates its environment through growth. *Sci. Robot.* **2**, eaan3028 (2017).
8. C. D. Woodruff, G. E. Woodruff, US Patent 9,267,640 (2016).
9. F. Collins, M. Yim, "Design of a spherical robot arm with the spiral zipper prismatic joint" in *2016 IEEE International Conference on Robotics and Automation (ICRA)* (IEEE, 2016), pp. 2137–2143.
10. S. J. Keating, J. C. Leland, L. Cai, N. Oxman, Toward site-specific and self-sufficient robotic fabrication on architectural scales. *Sci. Robot.* **2**, eaam8986 (2017).
11. T. G. Chen, S. Newdick, J. di, C. Bosio, N. Ongole, M. Lapôtre, M. Pavone, M. R. Cutkosky, Locomotion as manipulation with ReachBot. *Sci. Robot.* **9**, eadi9762 (2024).
12. D. A. Spencer, B. Betts, J. M. Bellardo, A. Diaz, B. Plante, J. R. Mansell, The LightSail 2 solar sailing technology demonstration. *Adv. Space Res.* **67**, 2878–2889 (2021).
13. S.-J. Kim, D.-Y. Lee, G.-P. Jung, K.-J. Cho, An origami-inspired, self-locking robotic arm that can be folded flat. *Sci. Robot.* **3**, eaar2915 (2018).
14. X. Zhang, R. Nie, Y. Chen, B. He, Deployable structures: Structural design and static/dynamic analysis. *J. Elast.* **146**, 199–235 (2021).
15. E. Groskopfs, US Patent 3,434,674 (1969).
16. J. M. Fernandez, "Advanced deployable shell-based composite booms for small satellite structural applications including solar sails" in *International Symposium on Solar Sailing 2017*, NF1676L-25486 (2017).
17. F. Rehnmark, M. Pryor, B. Holmes, D. Schaechter, N. Pedreiro, C. Carrington, "Development of a deployable nonmetallic boom for reconfigurable systems of small spacecraft" in *48th AIAA/ASME/ASCE/AHS/ASC Structures, Structural Dynamics, and Materials Conference* (AIAA, 2007), p. 2184.
18. L. Nicholson, M. W. Folkers, T. W. Murphey, "Rollable composite boom and deployer mechanism technologies" in *AIAA SCITECH 2022 Forum* (AIAA, 2022), p. 1118.
19. F. Roybal, J. Banik, T. Murphey, "Development of an elastically deployable boom for tensioned planar structures" in *48th AIAA/ASME/ASCE/AHS/ASC Structures, Structural Dynamics, and Materials Conference* (AIAA, 2007), p. 1838.
20. H. Yang, H. Guo, Y. Wang, J. Feng, D. Tian, Analytical solution of the peak bending moment of an M boom for membrane deployable structures. *Int. J. Solid Struct.* **206**, 236–246 (2020).
21. J. M. Fernandez, C. E. Volle, "Corrugated rollable tubular booms" in *AIAA Scitech 2021 Forum* (AIAA, 2021), p. 0296.
22. M. Thaker, S. J. Joshi, H. Arora, D. B. Shah, Tape spring for deployable space structures: A review. *Adv. Space Res.* **73**, 5188–5219 (2024).
23. S. Pellegrino, Deployable structures. *J. Int. Assoc. Shell Spat. Struct.* **39**, 175–188 (1998).
24. B. Suthar, S. Jung, Design and bending analysis of a metamorphic parallel twisted-scissor mechanism. *J. Mech. Robot.* **13**, 040901 (2021).
25. C. Leclerc, L. L. Wilson, M. A. Bessa, S. Pellegrino, "Characterization of ultra-thin composite triangular rollable and collapsible booms" in *4th AIAA Spacecraft Structures Conference* (AIAA, 2017), p. 0172.
26. N. Katsumata, M. Kume, K. Higuchi, Deployment behavior control using cables and bi-shape memory alloy convex tape booms. *Adv. Mech. Eng.* **9**, 10.1177/1687814017707909 (2017).
27. J. M. Fernandez, US Patent 9,863,148 (2018).
28. M. Arya, N. Lee, S. Pellegrino, Crease-free biaxial packaging of thick membranes with slipping folds. *Int. J. Solid Struct.* **108**, 24–39 (2017).
29. I. Running, C. Wright, R. J. Lang, L. Howell, S. Magleby, Origami folding pattern development for gossamer structures. *Int. J. Mech. Sci.* **285**, 109780 (2025).
30. Y. Chen, R. Peng, Z. You, Origami of thick panels. *Science* **349**, 396–400 (2015).
31. T. G. Nelson, T. K. Zimmerman, S. P. Magleby, R. J. Lang, L. L. Howell, Developable mechanisms on developable surfaces. *Sci. Robot.* **4**, eaau5171 (2019).
32. D.-Y. Lee, J.-K. Kim, C.-Y. Sohn, J.-M. Heo, K.-J. Cho, High–load capacity origami transformable wheel. *Sci. Robot.* **6**, eabe0201 (2021).
33. S. Felton, M. Tolley, E. Demaine, D. Rus, R. Wood, A method for building self-folding machines. *Science* **345**, 644–646 (2014).
34. D. Melancon, B. Gorissen, C. J. García-Mora, C. Hoberman, K. Bertoldi, Multistable inflatable origami structures at the metre scale. *Nature* **592**, 545–550 (2021).
35. Y. Zhu, E. T. Filipov, Large-scale modular and uniformly thick origami-inspired adaptable and load-carrying structures. *Nat. Commun.* **15**, 2353 (2024).
36. R. J. Wood, S. Avadhanula, R. Sahai, E. Steltz, R. S. Fearing, Microrobot design using fiber reinforced composites. *J. Mech. Des.* **130**, 052304 (2008).
37. M. Sakovsky, I. Maqueda Jimenez, C. Karl, S. Pellegrino, J. Costantine, "Dual-matrix composite wideband antenna structures for cubesats" in *2nd AIAA Spacecraft Structures Conference* (AIAA, 2015), p. 0944.
38. J. P. Whitney, P. S. Sreetharan, K. Y. Ma, R. J. Wood, Pop-up book MEMS. *J. Micromech. Microeng.* **21**, 115021 (2011).
39. J. R. Cannon, C. P. Lusk, L. L. Howell, "Compliant rolling-contact element mechanisms" in *International Design Engineering Technical Conferences and Computers and Information in Engineering Conference* (2005), vol. 47446, pp. 3–13.
40. M. Hillebrandt, M. E. Zander, C. Huehne, Sliding core deployment mechanism for solar sails based on tubular shell masts, paper presented at 5th International Symposium on Solar Sailing, Aachen, Germany, 30 July to 2 August 2019.
41. T. K. Saito, K. Onodera, R. Seino, T. Okawa, Y. Saito, 300-N class convex-based telescopic manipulator and trial for 3-DOF parallel mechanism robot. *J. Robot. Mechatron.* **33**, 141–150 (2021).
42. P. Vacharajittiphan, S. Woolcock, N. S. Trahair, Effect of in-plane deformation on lateral buckling. *J. Struct. Mech.* **3**, 29–60 (1974).
43. S.-s. Cheng, B. Kim, L.-y. Li, Lateral–torsional buckling of cold-formed channel sections subject to combined compression and bending. *J. Constr. Steel Res.* **80**, 174–180 (2013).
44. R. Bruins, "Lateral torsional buckling of laterally restrained steel beams," thesis, Eindhoven University of Technology, Eindhoven, Netherlands (2007).
45. R. E. Erkmen, M. M. Attard, Lateral–torsional buckling analysis of thin-walled beams including shear and pre-buckling deformation effects. *Int. J. Mech. Sci.* **53**, 918–925 (2011).
46. F. Zhang, M.-Y. Kim, A simple but accurate FEM for lateral-torsional buckling loads of mono-symmetric thin-walled beams considering pre-buckling effects. *Thin-Walled Struct.* **206**, 112676 (2025).
47. T. Ludvigsen, Hangprinter v4 manual (2024); https://hangprinter.org/doc/v4/.
48. T. Ludvigsen, Hangprinter Gitlab (2024); https://gitlab.com/tobben/hangprinter/.
49. M. H. Ang, W. Wei, L. Teck-Seng, "On the estimation of the large deflection of a cantilever beam" in *Proceedings of IECON'93-19th Annual Conference of IEEE Industrial Electronics* (IEEE, 1993), pp. 1604–1609.
50. J. Song, Code for deployable 3D printing mobile robotic system, Zenodo (2024); https://zenodo.org/records/14166163.


**Acknowledgments:** We thank J. Yang and the members of the Biorobotics Laboratory for the helpful discussions and feedback on the paper. In addition, we thank T. Ludvigsen. **Funding:** This work was supported by the National Research Foundation of Korea (NRF) Grant funded by the Korean Government (MSIT) (RS-2023-00208052) (K.-J.C.). **Author contributions:** Conceptualization: S.-P.J., J.S., C.K., and K.-J.C. Methodology: S.-P.J., J.S., and K.-J.C. Investigation: S.-P.J., J.S., C.K., H.L., I.J., and J.K. Visualization: S.-P.J., J.S., and C.K. Funding acquisition: K.-J.C. Supervision: S.-P.J., J.S., K.-J.C., and H.L. Writing—original draft: S.-P.J., J.S., C.K., and K.-J.C. Writing—review and editing: S.-P.J., J.S., and K.-J.C. **Competing interests:** S.-P.J., J.S., and K.-J.C. are inventors on a Korean patent (KR 10-2569390) and an international patent application (PCT/KR2024/002895) held/submitted by the SNU R&DB Foundation. The other authors declare that they have no competing interests. **Data and materials availability:** All data needed to support the conclusions of this manuscript are included in the main text or Supplementary Materials. For the code of the deployable 3D-printing mobile robotic system, the 3D-printing code is available online (*48*), and the mobile robotic system code is available on Zenodo (https://doi.org/10.5281/zenodo.14166163).

Submitted 19 December 2024
Accepted 28 October 2025
Published 26 November 2025
10.1126/scirobotics.adv4696

Science Robotics

# Foldable and rollable interlaced structure for deployable robotic systems

Sun-Pill Jung, Jaeyoung Song, Chan Kim, Haemin Lee, Inchul Jeong, Jongmin Kim, and Kyu-Jin Cho

*Sci. Robot.* **10** (108), eadv4696. DOI: 10.1126/scirobotics.adv4696







*Science Robotics* (ISSN 2470-9476) is published by the American Association for the Advancement of Science. 1200 New York Avenue NW, Washington, DC 20005. The title *Science Robotics* is a registered trademark of AAAS.